Journal of Marine Science and Application (2026) 25: 550-560
https://doi.org/10.1007/s11804-025-00754-w

RESEARCH ARTICLE

Ultimate Bearing Characteristics Analysis of a Novel Anchor Structure for Floating Offshore Wind Turbine under Mooring Line Failure Conditions

Conghuan Le[1], Xinting Zheng[1], Siteng Ma[1], Puyang Zhang[1] and Hongyan Ding[1]

Received: 17 March 2025 / Accepted: 29 July 2025

Abstract

This paper introduces a novel three-anchor combined suction anchor (TACSA) structure and evaluates the ultimate bearing characteristics of two mooring types under mooring line failure scenarios: single-primary-anchor mooring (SPAM) and dual-primary-anchor mooring (DPAM). Utilizing the finite element software ABAQUS, the ultimate bearing capacity and failure mode of the anchor were analyzed under the mooring line failure conditions. The findings indicate that with an increase in the deflection angle, the bearing capacity of the anchor experiences a gradual decline. A comparison of the two types of mooring revealed that DPAM resulted in a reduced descending speed of the bearing capacity and a smaller deflection angle of the anchor compared to the SPAM. In the SPAM system, the occurrence of linear plastic damage is contingent upon the attainment of a deflection angle of 45°. In the DPAM system, such damage manifests when the deflection angle exceeds 60°. These findings suggest that the synergistic effect between the anchors and the soil is enhanced in the DPAM system. Consequently, DPAM system demonstrates superior ultimate bearing characteristics and a reduced rotation degree, rendering it more effective in resisting the torque load induced by the deflection angle compared to SPAM system.

Keywords Offshore wind power; Bearing capacity; Failure modes; Three-anchor combined suction anchor; Mooring types

1 Introduction

To achieve the goal of carbon peaking and carbon neutrality, China is actively promoting the low-carbon transformation of the energy structure. This is particularly evident in the domain of wind power, which has witnessed continuous technological advancements and policy developments. As a result, offshore wind power has emerged as a pivotal component of China's energy transformation. Notably, floating offshore wind turbines (FOWTs), as a key innovation in offshore wind technology, hold immense potential to advance the development of deep-water offshore wind power (Le et al., 2020; Le et al., 2021; Wang et al., 2025).

As one of the critical components of floating offshore wind power systems, the suction anchor boasts several notable advantages, including a reduced steel volume, simplified sinking processes, enhanced recyclability, prolonged service life, and substantial bearing capacity (Zhao et al., 2020; Wang et al., 2019b). It has become a relatively mature and widely used anchor type in several deep-sea projects (Ehlers et al., 2004; Wang and Pang, 2011; Hu et al., 2022; Zhang et al., 2023; Zhang et al., 2024). A suction anchor consists of a hollow cylinder with a top lid and a bottom opening. The outer diameter of a suction anchor typically ranges from 2.5 to 12 m. Research on suction anchors encompasses a range of methodologies, including theoretical analysis, small-scale model tests, centrifuge tests, in-situ soil tests, and finite element analysis (Andersen et al., 2005; Li, 2025). The three-anchor combined suction anchor (TACSA) is a recently developed type of suction anchor. The utilization of a stable triangular geometry has been demonstrated to enhance its anti-pull and anti-torque bearing capacity, while concurrently reducing its weight, thereby facilitating transportation and installation

Article Highlights

- Floating wind turbine research is undergoing rapid development. The design of offshore anchor systems has the potential to facilitate the expansion of offshore wind energy development.
- The research on the ultimate bearing characteristics under mooring line failure helps optimize the design of offshore anchor systems, including the anchor structures and the mooring types.
- The implementation of a novel anchoring system has the potential to enhance the safety and stability of floating offshore wind turbine engineering.
- Two mooring types are presented and subsequently compared. The performance of each mooring type is contingent upon its bearing capacity and failure mode.

✉ Conghuan Le
leconghuan@163.com

[1] State Key Laboratory of Hydraulic Engineering Intelligent Construction and Operation, Tianjin University, Tianjin 300072

(Wang and Pang, 2011). Presently, TACSA systems have been utilized in practical engineering projects internationally, as evidenced in Figure 1(b). However, research showing their bearing characteristics remains limited.

(a) Single-anchor structure (b) Three-anchor structure

Figure 1 Form of suction anchor structure

A comparison of single suction anchors and TACSA reveals that the latter incur slightly higher costs in transportation and installation, yet the increase is relatively modest. Each anchor in the TACSA structure is smaller than a single suction anchor. For the same bearing capacity, the entire structure has smaller dimensions than a single suction anchor. Conversely, the TACSA is installed in a manner similar to that of a single suction anchor. Given the established mature of single-anchor installation, this approach mitigates the risk of substantial cost escalation. A cost-benefit analysis indicates that, while the TACSA system incurs additional expenses related to transportation, installation, and construction when compared with the single suction anchor system, these increased costs are within reasonable limits and offer certain economic advantages.

Because of the complex marine environment, which includes elements such as strong winds, huge waves, sea currents, and aging parts, the mooring system may suffer damage (Bae and Kim, 2015; Bae et al., 2017). Should an anchor chain be severed, the remaining intact chain will abruptly encounter a substantial force, resulting in a deflection of the load direction at the mooring point on the anchor (Ali et al., 2025). In this case, the bearing capacity (Rui et al., 2023; Rui et al., 2024; Yan et al., 2024) and failure mode (Ibsen et al., 2014; Cheng et al., 2021) of the anchor need to be considered. Consequently, it is imperative to establish mooring line failure scenarios to assess the bearing capacity and failure mode of the anchor.

Sukumaran et al. (1999) conducted a study on the relationship between the ultimate bearing capacity of suction anchors in soft clay and the position of mooring points. At the maximum ultimate bearing capacity, the suction anchor experiences only translation, with no rotation. By positioning the mooring point at the top of the anchor, rotation can be effectively mitigated, thereby enhancing the ultimate bearing capacity. In their seminal study, Zhang et al. (2011) utilized the finite element software ABAQUS to investigate the impact of mooring point position and the length-to-diameter ratio of suction anchors on their ultimate bearing capacity, as well as to elucidate the instability modes of deep-sea suction anchors. The position of the mooring point exerts a significant influence on the ultimate bearing capacity and stability of the suction anchor. Changes in the mooring point position can induce instability, including forward rotation, translational sliding, and backward rotation. The instability mode is also influenced by the length-to-diameter ratio. Wang et al. (2012) analyzed the influence of different loading directions on the failure modes and ultimate bearing capacities. The failure modes remain vertical pullout, and the primary factor influencing the ultimate bearing capacity is the reverse end-bearing resistance at the anchor tip. However, lateral displacements and ultimate bearing capacities exhibit a substantial increase when the loading direction varies from 40° to 20° for suction anchors with inclined loads at the optimal load attachment point. Liu and Wang (2013) examined the failure mode of suction anchors and developed a method for analyzing the bearing capacity of suction anchors using finite element method. The interaction between the anchor and soil is determined by the anchor's failure mode. In the event of anchor failure mode as a vertical pullout, the utilization of a critical shear stress friction model is deemed appropriate for the purpose of delineating the interaction between anchor and soil. In the event of anchor failure mode as designated by lateral failure, the Coulomb friction model is deemed an appropriate means to describe the interaction between anchor and soil. Wang et al. (2019a) developed three-dimensional finite element models of suction anchors using ABAQUS software platform. The present study investigates the effect of mooring point position, mooring direction, and anchor depth on the ultimate bearing capacity of suction anchors. Faizi et al. (2020) presented a closed-form model to estimate the lateral bearing capacity of caisson foundations for offshore wind turbines (OWTs). The proposed solution has demonstrated the capacity to provide a superior estimate of the lateral bearing capacity of caissons in comparison to existing models.

This paper primarily analyzes the bearing characteristics analysis of a novel TACSA for floating offshore wind turbines (FOWTs) under mooring line failure conditions. Two mooring types are designed for this special three-anchor structure: single-primary-anchor mooring (SPAM) and dual-primary-anchor mooring (DPAM). The analysis of the TACSA's ultimate bearing characteristics under the

mooring line failure condition is instrumental in the optimization of anchor design and the enhancement of its safety and stability. Two mooring types will result in different force distributions on the TACSA structure under the mooring line failure condition, thereby leading to differences in bearing capacity and failure modes. In order to explore the advantages and disadvantages of two mooring types and optimize the anchorage design under the mooring line failure condition, it is necessary to study their bearing characteristics respectively. Therefore, the aim of this paper is to study the ultimate bearing characteristics of two mooring types under mooring chain failure scenarios.

2 TACSA model

The finite element software ABAQUS was utilized to construct a TACSA model, with the Mohr-Coulomb model selected for the soil simulation. The dimensions of the TACSA structures were determined based on the specific working conditions, with each structure exhibiting distinct dimensions. Following preliminary calculations and a comprehensive consideration of both bearing capacity and construction cost-effectiveness, it was determined that the subsequent analysis will be based on the dimensions. The length-to-diameter ratio (L/D) of the TACSA is 6, and the distance-to-diameter ratio (S/D)-defined as the ratio of the clear distance between two adjacent anchors in TACSA to the anchor diameter- is 0.1. Additionally, the mooring point is positioned 7.2 m below the top of the anchor (3/5 of the anchor's height), as this location has been identified as the optimal mooring point in prior studies.

The model's configuration is depicted in Figure 2, with an anchor height (L) of 12 m and single anchor diameter (D) of 2 m, and clear distance between adjacent single anchors (S) is 0.2 m. The three single anchors within TACSA have identical dimensions and are arranged in a regular triangular configuration. The reference point (RP) is established and subsequently coupled with the anchor. The load is applied to the reference point to simulate the force of the mooring line on the anchor. For SPAM, loads are applied to reference point 2 (RP2). RP2 component is situated at the core of the primary anchor surface, with a distance of 7.2 m below the anchor's top. For DPAM, loads are applied to reference point 1 (RP1). The location of RP1 is precisely defined as being horizontally centered between the two primary anchors, with a distance of 7.2 m measured from the top of anchor. To eliminate the influence of boundary conditions on the bearing capacity of suction anchors, the soil is modeled as a rectangular prism with a side length of 30 m (15D) and a height of 36 m (3L), as stated in the literature of Lv et al. (2005). The bottom surface of the soil is fully constrained, and the side surface is horizontally constrained. The soil within the suction anchor is meticulously shaped to mirror the anchor's geometry, with its base securely tied to the surrounding soil. The friction between the soil and the suction anchor is simulated by establishing contacts. The soil surface within the anchor is in direct contact with the inner wall of the anchor. The inner wall of the anchor is designated as the master surface, while the soil surface within the anchor is considered the slave surface. The soil surface external to the anchor is in direct contact with the outer wall of the anchor. The outer wall of the anchor is designated as the master surface, while the soil surface external to the anchor is considered the slave surface. It has been determined that the mesh of the inner and surrounding soil of the TACSA model, which are the stress concentration areas, must be refined (Luan, 2023). The mesh size of the soil in contact with the anchor's top is set to 0.2 m, and the mesh size in height direction of the soil in contact with the anchor's wall is set to 0.8 m. It is noteworthy that the mesh size of the anchor is consistent with the mesh size of the soil. And the selected mesh density ensures both computational accuracy and computational efficiency.

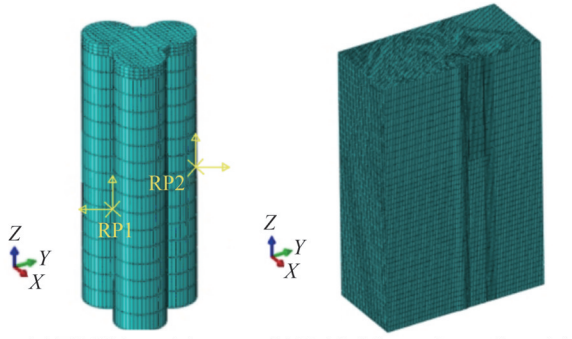

(a) TACSA model (b) Half of the anchor-soil model

Figure 2 Finite element model

In finite element calculations, clay was selected for the soil analysis. The specific soil parameters are presented in Table 1.

Table 1 Main parameters of soil

soil	ρ (kg/m^3)	E (kPa)	v	S_u (kPa)
clay	1 600	2 500	0.49	5

To verify the effectiveness of the finite element model, a three-dimensional finite element model with an L/D ratio of 1 was created. The diameter D of the suction anchor is 5 m, and its length L is 5 m, as illustrated in Figure 3. To adequately eliminate boundary effects, the diameter of the soil model is set to 5D, and the height is set to 3L.

The calculated result indicates an ultimate horizontal bearing capacity of 457 kN, N_h = 3.7, and the error margin between the results and the calculation of Taiebat and

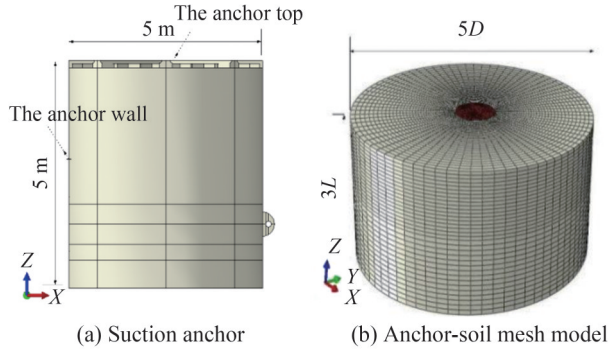

(a) Suction anchor (b) Anchor-soil mesh model

Figure 3 Finite element model

Carter (2005) is 7.5%. The ultimate vertical bearing capacity is 1 490 kN, and the error margin is 4‰. The ultimate torque bearing capacity is 1 101 kNm, and the error margin is 7%. The finite element simulation results have been validated, as evidenced by the fact that both error margins are within 7.5%.

3 Principle and method

3.1 Mohr–Coulomb model

The Mohr–Coulomb plastic model is extensively utilized in geotechnical engineering, primarily for granular materials under monotonic loading. The yield surface function for the Mohr–Coulomb model is as follows:

$$F = R_{mc}q - p\tan\varphi - c = 0 \tag{1}$$

where φ is the tilt angle of the material yield surface on the q-p stress surface, $0° \leqslant \varphi \leqslant 90°$, c is the cohesion of the material, and $R_{mc}(\Theta, \varphi)$ is the deviatoric stress coefficient, which determines the shape of the Mohr-Coulomb yield surface in the π plane.

The formula for $R_{mc}(\Theta, \varphi)$ is:

$$R_{mc} = \frac{1}{\sqrt{3}\cos\varphi}\sin\left(\Theta + \frac{\pi}{3}\right) + \frac{1}{3}\left(\Theta + \frac{\pi}{3}\right)\tan\varphi \tag{2}$$

where Θ is the polar deflection angle, the formula of Θ is:

$$\cos(3\Theta) = \left(\frac{r}{q}\right)^3 \tag{3}$$

where r is the third invariant of stress deviator.

As illustrated in Figure 4, the shapes of the Mohr–Coulomb yield surface on the meridian and π planes are depicted, thus elucidating the relationships between the Mohr–Coulomb yield surface, Rankine yield surface, Tresca yield surface, and Drucker-Prager yield surface.

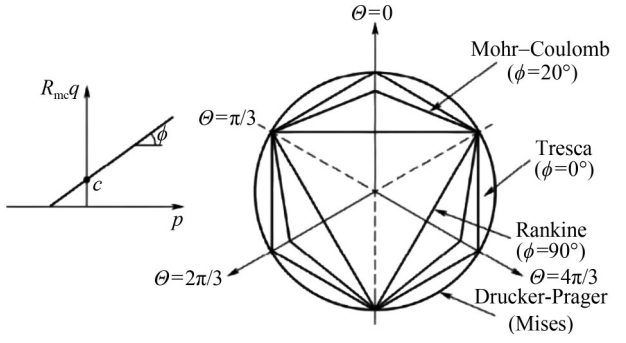

Figure 4 Yield surface of the Mohr–Coulomb model

3.2 Loading method and ultimate bearing capacity determination criterion

The fixed displacement ratio method, proposed by Bransby and Randolph (1997), is employed to apply loading to the anchor model. This method involves directly applying displacement loads in different directions at the anchor load application point to obtain the V-H load envelope. The displacement-load curve via finite element numerical simulation, and the method for determining the ultimate bearing capacity proposed by Villalobos (2006) is employed. As demonstrated in Figure 5, tangents are derived at the onset of the elastic stage and the end of the plastic stage of the curve. The two tangents intersect at a point, and a horizontal line is drawn from this intersection to the curve. The intersection of the horizontal line and the curve is defined as the ultimate state of the anchor. The corresponding load at this point is referred to as the ultimate bearing capacity.

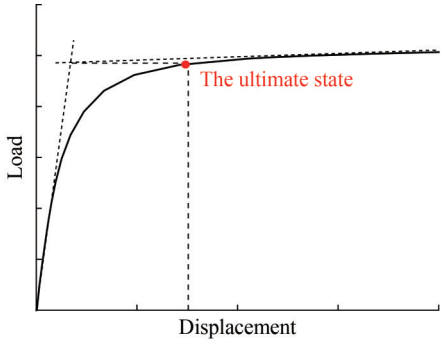

Figure 5 Determination criterion of ultimate bearing capacity

4 Analysis of the ultimate bearing characteristic under the mooring line failure condition

Presently, floating wind turbines are typically moored with 3-9 suction anchors. In the event of a mooring line failure due to breakage, the magnitude and direction of the loads on the remaining chains undergo a change. This

change leads to alterations in the load direction at the mooring points on the anchors and affects their ultimate bearing capacity. To ascertain the bearing capacity of the anchors under mooring line failure conditions, it is assumed that the load on the mooring points of the remaining anchors is applied at angles of 15°, 30°, 45°, 60°, and 75° relative to the vertical plane. Each load direction is horizontally deflected by 7.5°, 10°, 20°, 30°, 40°, and 60° from a reference direction.

Figure 6 presents a top-down view of the TACSA model for the two mooring types. Figure 6(a) illustrates the mooring configuration in which the mooring line is attached to a single primary anchor (designated as SPAM). This arrangement subdivides the TACSA model into a primary anchor and two auxiliary anchors. The auxiliary anchor located in proximity to the load deflection direction is designated as "auxiliary anchor #1" while the one positioned distant from the load deflection direction is referred to as "auxiliary anchor #2". Figure 6(b) illustrates the mooring configuration in which the mooring line is attached to two primary anchors (designated as DPAM). This configuration subdivides the TACSA model into two primary anchors and one auxiliary anchor. The primary anchor, situated in proximity to the load deflection direction, is designated as "primary anchor #1", while the other primary anchor, positioned away from the load deflection direction, is designated as "primary anchor #2". The dashed line arrow indicates the load direction of the anchor is under intact mooring line conditions, while the solid line arrow indicates the load direction of the anchor under the mooring line failure condition. In this context, θ denotes the load deflection angle.

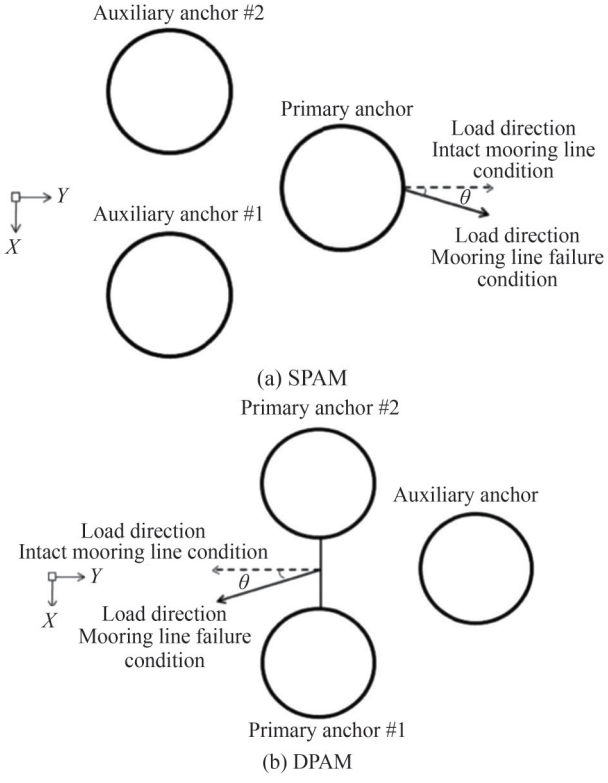

Figure 6 Loading diagram of the TACSA model

4.1 Ultimate bearing capacity

In this section, loads are applied at the mooring point at angles of 15°, 30°, 45°, 60°, and 75° relative to the vertical plane. Each of these load directions is deflected horizontally by 7.5°, 10°, 20°, 30°, 40°, and 60°. The bearing capacity of the anchor is calculated via numerical simulation, and the results were compared with that when the deflection angle θ is 0°. The relationship between the deflection angle θ and the bearing capacity is analyzed.

Figures 7 and 8 illustrate the displacement-load curves for the two mooring types, respectively. Plots representing various loading angles are included in each figure, with seven displacement-load curves per angle, one for each horizontal deflection angle. The ultimate bearing capacity of the TACSA under the 0° deflection angle is designated as F_{max}, and the ultimate bearing capacity under the other deflection angles is designated as F, thus resulting in the normalized ultimate load curves. The results of the study are as follows: 1) With an increase in the deflection angle θ, the bearing capacity of the TACSA gradually decreases. 2) When the deflection angle θ is no greater than 30°, the ratios of F to $\underline{F}_{max}$ for both SPAM and DPAM are greater than 0.98. At this time, the deflection angle exerts minimal influence on the ultimate bearing capacity of the TACSA. 3) When the deflection angle θ undergoes a change from 40° to 60°, as shown in Figure 7(a), the force F changes from 0.94 F_{max} to 0.84 F_{max}, resulting in a substantial decrease in the ultimate bearing capacity for SPAM. Similarly, when the deflection angle θ varies from 40° to 60°, as shown in Figure 8(a), the force $\underline{F}$ changes from 0.96 F_{max} to 0.92 F_{max}, leading to a modest decrease in the ultimate bearing capacity for DPAM. 4) When the deflection angle is 60°, the ratios of F to F_{max} for DPAM range from 0.92 to 0.94, as shown in Figure 8, which is significantly higher than those for SPAM. Therefore, compared with SPAM, DPAM is advantageous in terms of resisting the torque load that is caused by the deflected mooring line.

4.2 Failure mode

4.2.1 Anchor displacement vectors

In this section, the load is applied at the mooring point at an angle of 15° from the vertical plane. The load direction is subsequently deflected horizontally by 0°, 15°, 30°, 45°, and 60°. As illustrated in Figures 9 and 10, these diagrams are the anchor-soil displacement vector contour diagrams. For SPAM, the mooring direction is aligned with the positive Y axis, and the loading direction rotates into the first quadrant when deviating from the original angle. For DPAM, the mooring direction is oriented along the

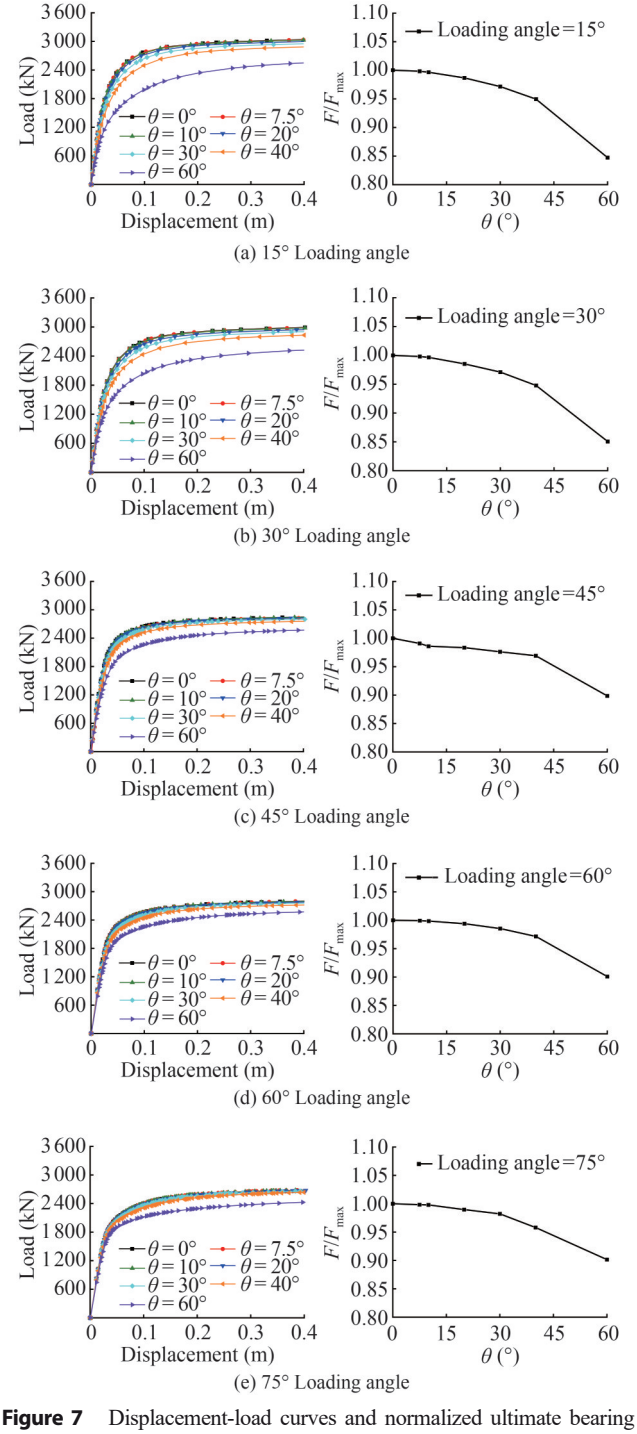

(a) 15° Loading angle
(b) 30° Loading angle
(c) 45° Loading angle
(d) 60° Loading angle
(e) 75° Loading angle

Figure 7 Displacement-load curves and normalized ultimate bearing capacity plots for SPAM

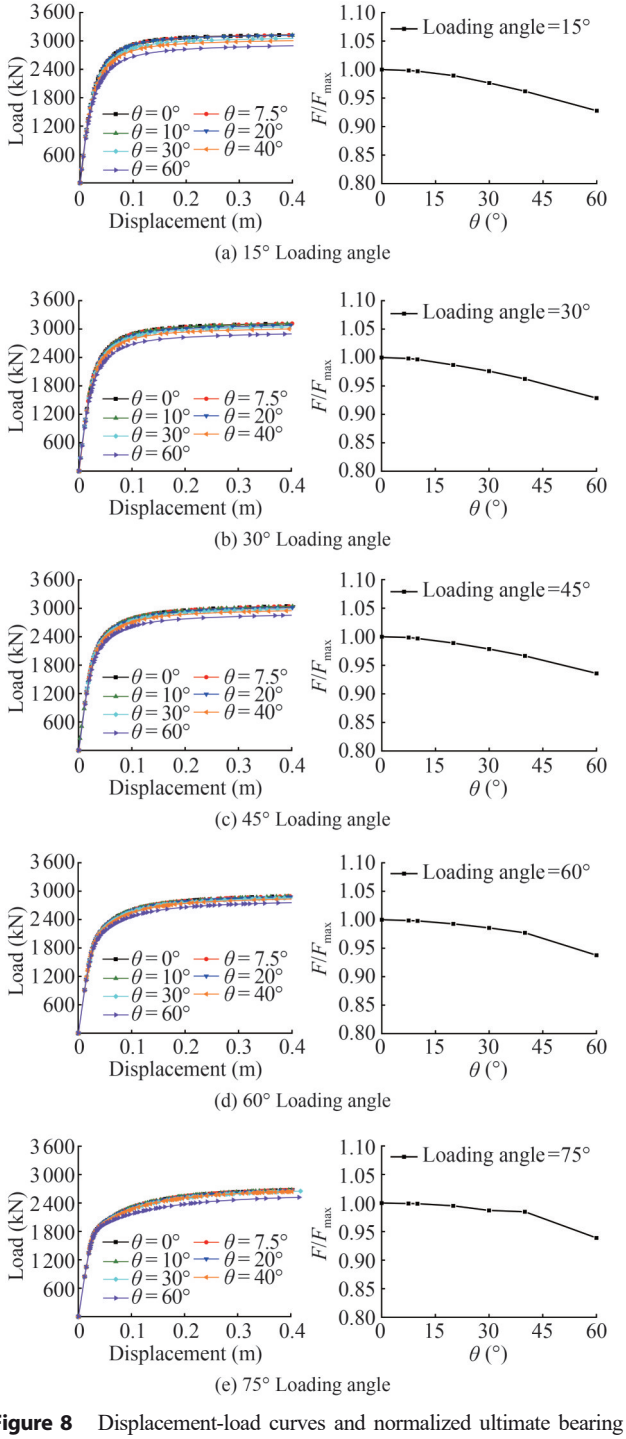

(a) 15° Loading angle
(b) 30° Loading angle
(c) 45° Loading angle
(d) 60° Loading angle
(e) 75° Loading angle

Figure 8 Displacement-load curves and normalized ultimate bearing capacity plots for DPAM

negative Y axis, and the loading direction rotates into the fourth quadrant when deviating from the original angle. As illustrated in Figure 9, the SPAM configuration secures the floating wind turbine. An increase in the deflection angle indicates an expansion of the anchor-soil gap on the left side of the primary anchor and the posterior side of the auxiliary anchor #2. As illustrated in Figure 10, for the DPAM, as the deflection angle increases, the X-direction force component increases, while the Y-direction force component decreases. Consequently, the anchor-soil separation gap on the left side of the auxiliary anchor and the primary anchor #2 expands. Comparing the displacement vectors of SPAM and DPAM reveals that the maximum displacement vector of DPAM is smaller than that of SPAM at deflection angles of 0°, 15°, 30°, and 45°. The TACSA with DPAM can distributes the load more uni-

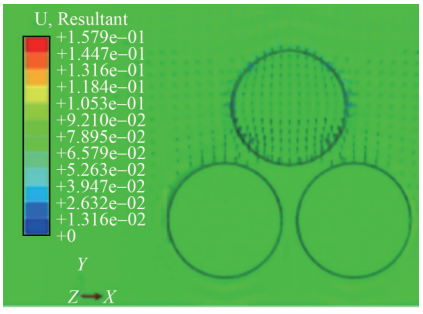

(a) 0° Deflection angle

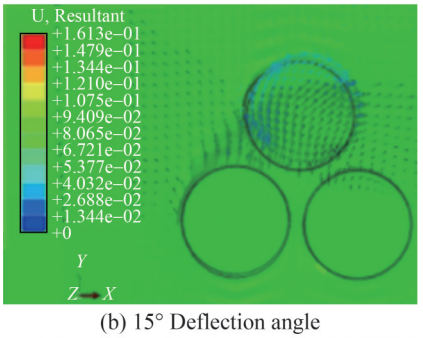

(b) 15° Deflection angle

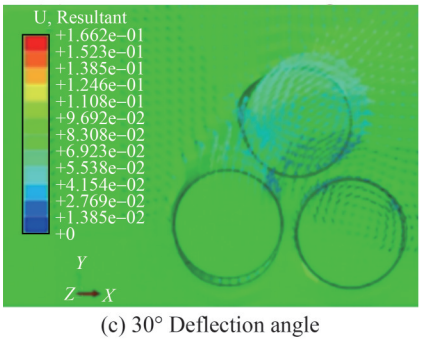

(c) 30° Deflection angle

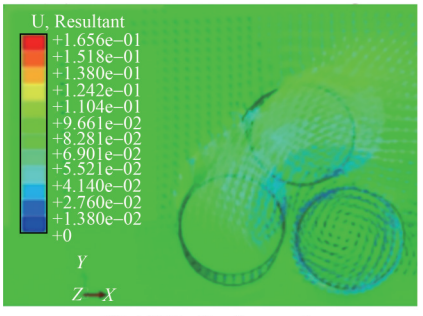

(d) 45° Deflection angle

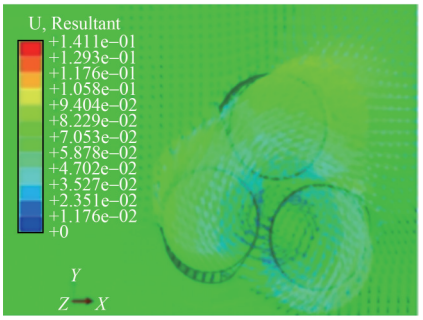

(e) 60° Deflection angle

Figure 9 Anchor displacement vector for SPAM

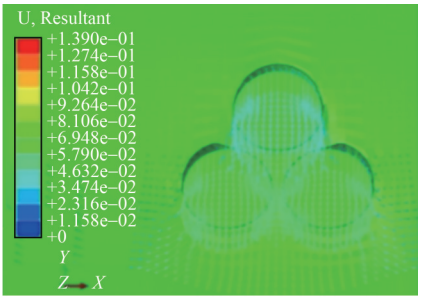

(a) 0° Deflection angle

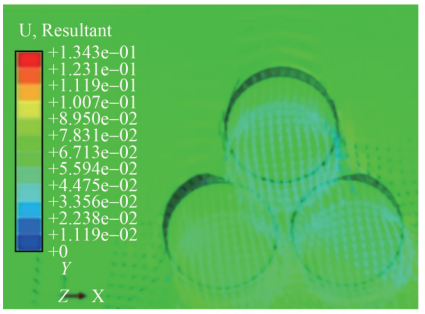

(b) 15° Deflection angle

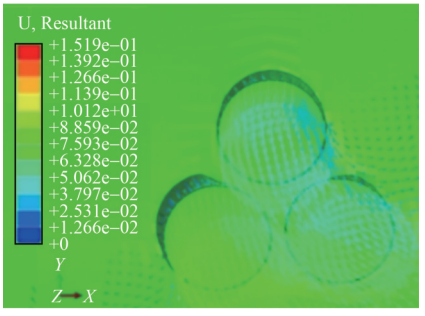

(c) 30° Deflection angle

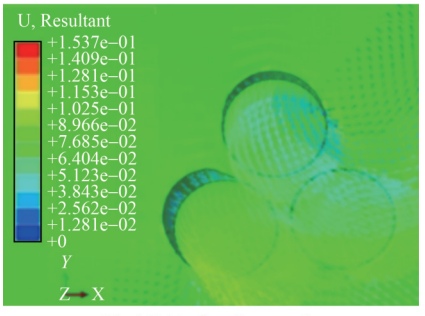

(d) 45° Deflection angle

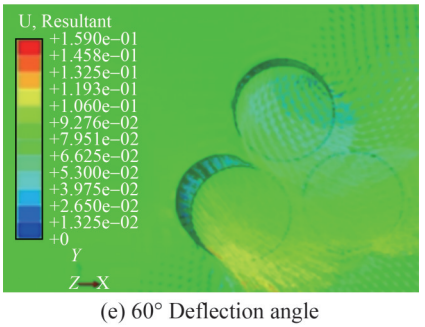

(e) 60° Deflection angle

Figure 10 Anchor displacement vector for DPAM

formly across the structure, thereby resulting in smaller displacement vectors and offering enhanced resistance to loads.

In the event that two mooring types (SPAM and DPAM) bear substantial loads and gradually reach the ultimate failure state, the anchor body deflects at an angle away from its central axis. The deflection angles are presented in Table 2. In the ultimate state, a comparison of the anchor's deflection angle of two mooring types reveals that the latter (DPAM) exhibits a lower degree of rotation and is more effective at resisting torque loads.

Table 2 Deflection angle of anchor away from central axis

Deflection angle from horizontal plane (°)	Angle deflection from center axis	
	SPAM (°)	DPAM (°)
15	0.39	0.47
30	0.84	0.69
45	1.34	1.06
60	1.61	1.48

4.2.2 Soil equivalent plastic strain

In this section, the load is applied at the mooring point at an angle of 15° from the vertical plane, and the load direction is subsequently deflected horizontally by 0°, 15°, 30°, 45°, and 60°. Figures 11 and 12 illustrate the soil equivalent plastic strain contour diagrams for the two mooring types. For SPAM, the mooring direction is aligned with the positive Y axis. For DPAM, the mooring direction is oriented along the negative Y axis. Furthermore, the load deflection direction rotates toward the positive X axis.

The results of the study are as follows: 1) For SPAM, when the deflection angle is 0°, the plastic failure area surrounding the primary anchor is distributed on both sides of the primary anchor. In contrast, the plastic failure area of the auxiliary anchor is located outside the auxiliary anchors. For DPAM, when the deflection angle is 0°, the plastic failure area of the primary anchors is situated on the outer side of the primary anchors, while the plastic failure area of the auxiliary anchor is distributed on both sides of the auxiliary anchor. 2) An increase in the deflection angle results in a shift in the plastic failure region. When the deflection angle reaches 60° , plastic failure is primarily concentrated on the primary anchor and auxiliary anchor #2 for SPAM. Conversely, for DPAM, plastic failure is concentrated on the primary anchor #2. 3) For SPAM, when the deflection angle reaches 45° , a plastic failure area emerges between the primary anchor and auxiliary anchor #2, extending from the seabed surface to the anchor bottom. For DPAM, when the deflection angle reaches 60°, a similar phenomenon is observed, manifesting as a plastic failure area extending from the seabed surface to the anchor bottom. This area is situated between the two primary anchors. Soil plastic failure areas are defined as the continuous plastic zone that is formed when the soil plastic strain

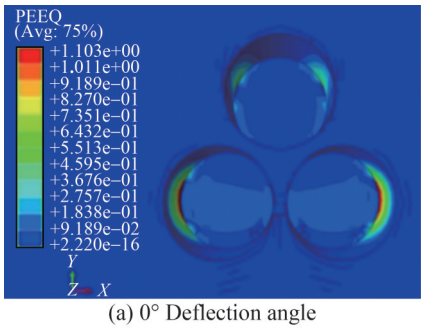

(a) 0° Deflection angle

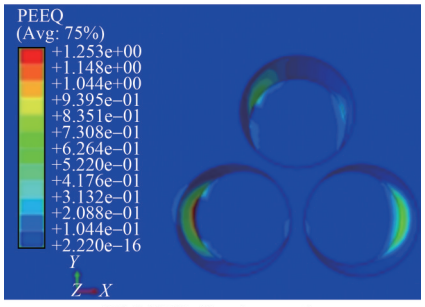

(b) 15° Deflection angle

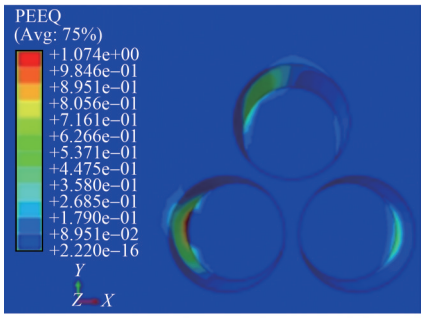

(c) 30° Deflection angle

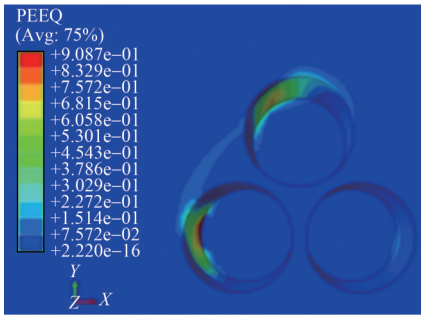

(d) 45° Deflection angle

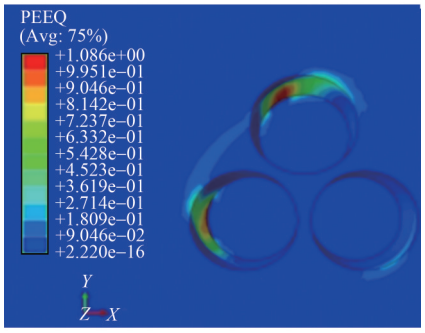

(e) 60° Deflection angle

Figure 11 Equivalent plastic strain contour diagrams for SPAM

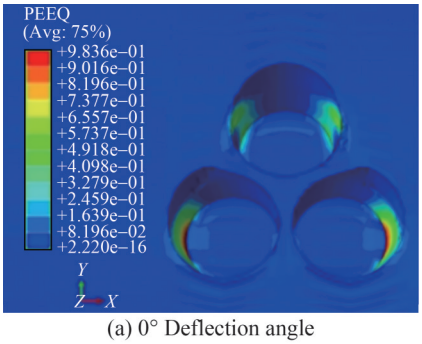

(a) 0° Deflection angle

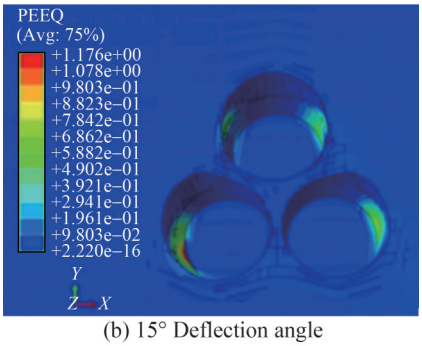

(b) 15° Deflection angle

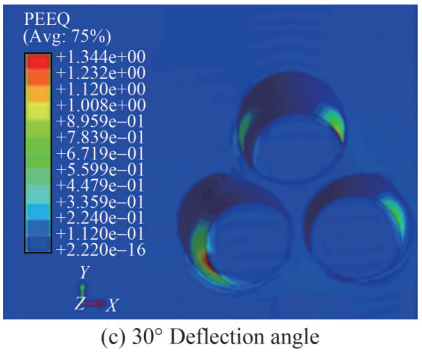

(c) 30° Deflection angle

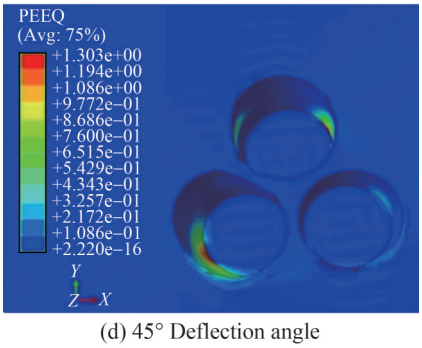

(d) 45° Deflection angle

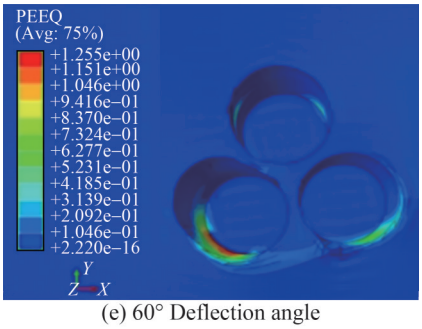

(e) 60° Deflection angle

Figure 12 Equivalent plastic strain contour diagrams for DPAM

reaches a specific threshold under loading. It is a critical factor in ascertaining soil stability. Yang et al. (2019) posited that the extent of the soil plastic zone should serve as the primary criterion for assessing instability, thereby supporting the notion that DPAM enhances stability. 4) As the anchor moves, the soil in the passive area around the anchors is compressed, resulting in an increase in earth pressure and equivalent plastic strain. A comparison between SPAM and DPAM reveals that when the deflection angle exceeds 30°, the soil plastic strain for DPAM is more pronounced. The correlation between the extent of equivalent plastic strain and the load-sharing ratio of soil which has been confirmed in the previous literature (Wu et al., 2025). This effect is known as the synergistic effect between anchor and soil. Consequently, DPAM exhibits a higher loading-bearing capacity.

5 Conclusion

The present study proposes a novel TACSA structure and two mooring types (SPAM and DPAM). The primary conclusions drawn from this analysis are as follows:

As the deflection angle increases, the bearing capacity of the TACSA decreases gradually. Notably, variations in the deflection angle exert minimal influence on the TACSA's ultimate bearing capacity when the deflection angle does not exceed 30° . However, as the deflection angle increases from 40° to 60°, the ultimate bearing capacity of SPAM decreases significantly, whereas that of DPAM only decreases slightly. It has been demonstrated that the ultimate bearing capacity of the latter is significantly higher than that of SPAM when the deflection angle is 60°. Consequently, DPAM exhibits superior resistance to torque loads induced by mooring line deflection relative to SPAM.

As the deflection angle increases, the anchor-soil separation gap on the left side of the primary anchor and on the back side of the auxiliary anchor #2 expands for SPAM. Conversely, for DPAM, the anchor-soil separation gap on the auxiliary anchor and on the left side of the primary anchor #2 expands progressively. A comparison of the displacement vectors of two mooring types reveals that the maximum displacement vector of DPAM is smaller than that of SPAM at deflection angles of 0°, 15°, 30°, and 45°. DPAM thus achieves smaller displacement magnitudes and offers greater advantages for load resistance. Additionally, a comparison of the anchor deflection angles of the two mooring types reveals that DPAM undergoes less rotational displacement, thereby exhibiting a superior torque loads resistance capacity.

For SPAM, when the deflection angle is 0°, the plastic failure area surrounding the primary anchor is distributed on both sides of the anchor. In contrast, the plastic failure area of the auxiliary anchor is situated on the outer side of

the anchor. For DPAM, the distribution of plastic failure areas are differs from that of SPAM. As the deflection angle increases, the plastic failure area undergoes a corresponding movement. At a deflection angle of 60°, the plastic failure in SPAM is primarily concentrated on the primary anchor and auxiliary anchor #2, while the plastic failure in DPAM is concentrated on the primary anchor #2. For SPAM, the plastic failure areas emerge when the deflection angle reaches 45°; for DPAM, the plastic failure area occurs when the deflection angle reaches 60°. Consequently, DPAM exhibits superior stability under mooring line failure conditions. As the anchor moves, the soil in the passive area is compressed, resulting in an increase in earth pressure and equivalent plastic strain. A comparison between SPAM and DPAM reveals that when the deflection angle exceeds 30°, the soil plastic strain in DPAM is more pronounced. This leads to an optimal synergistic effect between anchor and soil. Consequently, DPAM demonstrates a higher load-bearing capacity.

Competing interests The authors have no competing interests to declare that are relevant to the content of this article.

References

Ali A, Shi W, Wang SS, Haider R, Li X, Zhai HB, Leng SD, Han XL (2025) Dynamic analysis of a Tetra-Spar floating offshore wind turbine with different tendons failure scenario. Ocean Engineering, 323: 120607. https://doi.org/10.1016/j.oceaneng.2025.120607

Andersen KH, Murff JD, Randolph MF, Supachawarote C (2005) Suction anchors for deepwater applications. International symposium on frontiers in offshore geotechnics: 3-30. https://doi.org/10.1201/NOE0415390637.ch1

Bae YH, Kim MH (2015) The dynamic coupling effects of a MUFOWT (multiple unite floating offshore wind turbine) with partially broken blade. Journal of Ocean and Wind Energy 2(2): 89-97. https://doi.org/10.17736/jowe.2015.mkr01

Bae YH, Kim MH, Kim HC (2017) Performance changes of a floating offshore wind turbine with broken mooring line. Renewable Energy 101:364-375. https://doi.org/10.1016/j. renene.2016.08.044

Bransby M , Randolph M (1997) Shallow foundations subject to combined loadings. Computer Methods and Advances in Geomechanics. editor/J. X. Yuan. Vol. 3 Wuhan, China. ed. The Netherlands: CRC Press: 1947-1952. https://research-repository.uwa.edu.au/en/publications/shallow-foundations-subject-to-combined-loadings

Cheng L, Hossain MS, Hu Y, Kim YH , Ullah SN (2021) Failure envelope of suction caisson anchors subjected to combined loadings in sand. Applied Ocean Research 114: 102801. https://doi.org/10.1016/j.apor.2021.102801

Ehlers CJ, Young AG , Chen JH (2004) Technology assessment of deep-water anchors. Offshore technology conference: 1-17. https://doi.org/10.4043/16840-MS

Faizi K, Faramarzi A, Dirar S ,Chapman D (2020) Development of an analytical model for predicting the lateral bearing capacity of caisson foundations in cohesionless soils. Ocean Engineering 218: 108112. https://doi.org/10.1016/j.oceaneng. 2020.108112

Hu RG, Liu HJ, Wang XH, Zhao Z, Shi W (2022) Scour mechanism around umbrella suction anchor foundation for offshore wind turbine in waves. Acta Energiae Solaris Sinica 43(11): 242-252. https://doi.org/10.19912/j.0254-0096.tynxb. 2021-0490

Ibsen LB, Larsen KA, Barari A (2014) Calibration of failure criteria for bucket foundations on drained sand under general loading. Journal of Geotechnical and Geoenvironmental Engineering 140(7). https://doi.org/10.1061/(ASCE)GT.1943-5606.0000995

Le CH, Ren JY, Wang K, Zhang PY, Ding HY (2021) Towing performance of the submerged floating offshore wind turbine under different wave conditions. Journal of Marine Science and Engineering 9(6): 633. https://doi.org/10.3390/jmse9060633

Le CH, Zhang J, Ding HY, Zhang PY, Wang GL (2020) Preliminary design of a submerged support structure for floating wind turbines, Journal of Ocean University of China 19(6): 1265-1282. https://doi.org/10.1007/s11802-020-4427-z

Li JH, Sun JX, Zhang Z, ZT, Li ZF (2025) Comparative investigation of torsional interactive behaviours between suction anchors and clayey ground by centrifugal tests. Ocean Engineering 341: 122676. https://doi.org/10.1016/j.oceaneng.2025.122676

Liu JL , Wang JH (2013) Numerical analysis of failure mode and bearing capacity of suction anchors with taut mooring systems in soft clay. Ocean Engineering 31(4): 10-20. https://doi.org/ 10.16483/j.issn.1005-9865.2013.04.012

Luan YX, Tang XW, Ren YB, Zhang XW (2023) Numerical simulation of pore pressure development beneath suction anchor under undrained condition during uplift. Applied Ocean Research 140: 103713. https://doi.org/10.1016/j.apor.2023.103713

Lv WT, Wang YH, Leng WM (2005) Finite element analysis of interaction of stressed concrete pipe pile and soil. Rock and Soil Mechanics 26(S1): 154-158. https://doi. org/10.16285/j. rsm. 2005. s1.037

Rui SJ, Zhou WJ, Shen KM, Guo Z (2023) Review on seabed trenches induced by mooring lines and analyses of anchor bearing capacity. Journal of Marine Science and Application 22: 296-310. https://doi.org/10.1007/s11804-023-00333-x

Rui SJ, Wang LZ, Jostad HP, Zhou ZF, Guo Z (2024) Bearing performance of a novel caisson-plate gravity anchor. Géotechnique 75(5): 686-697. https://doi.org/10.1680/jgeot.23. 00451

Sukumaran B, Mccarron WO, Jeanjean P, Abouseeda H (1999) Efficient finite element techniques for limit analysis of suction caissons under lateral loads. Computers and Geotechnics 24(2): 89-107. https://doi.org/10.1016/S0266-352X(98)00036-6

Taiebat HA, Carter JP (2005) Interaction of forces on caissons in undrained soils. The Proceedings of the International Offshore and Polar Engineering Conference 15(0): 104-111. https://onepetro.org/ISOPEIOPEC/proceedings-abstract/ISOPE05/ISOPE05/ISOPE-I-05-217/9381

Villalobos Jara F (2006) Model testing of foundations for offshore wind turbines. University of Oxford. https://doi.org/10.5287/ ora-m8gaameyk

Wang LQ, Pang R (2011) The application of suction pile in the deepwater oil and gas field development engineering, Ship & Ocean Engineering 40(2): 98-103. https://doi. org/10.3963/j. issn. 1671-7953.2011.02.028

Wang JH, Liu JL, Chen WQ (2012) Effects of loading direction on ultimate bearing capacity of suction anchors with taut mooring system. Journal of Geotechnical Engineering 34(3): 385-391. https://www.cgejournal.com/en/article/pdf/preview/14509.pdf

Wang JZ, Ren YJ, Shi W, Collu M, Venugopal V, Li X (2025) Multi objective optimization design for a 15 MW semi-submersible

floating offshore wind turbine using evolutionary algorithm. Applied Energy 377: 124533. https://doi.org/10.1016/j.apenergy.2024.124533

Wang P, Wang XT, Zhang XF (2019a) Finite element analysis of bearing characteristics of suction anchor foundation in clay. Construction technology 48(S1): 24-28. DOI: CNKI:SUN:SGJS.0.2019-S1-005

Wang Y, Zhu XY, Yang Q (2019b) Installation of suction caissons and formation of soil plug considering variation of permeability of sand. Journal of Geotechnical Engineering 41(1): 184-190. https://dx.doi.org/10.11779/CJGE201901021

Wu QY, Wang C, Zhang H, Wang YK, Wang J, Liang FY (2025) Numerical investigation on the lateral behavior of scour-affected tripod foundation for offshore wind turbine with solidified soil remediation. Ocean Engineering 326: 120864. https://doi.org/10.1016/j.oceaneng.2025.120864

Yan B, Zhu WX, Gao B, Ye GL, Tian YH, Wang YF (2024) Bearing capacity analysis and mechanism study of shared caisson under multidirectional loading. Ocean Engineering 301: 117530. https://doi.org/10.1016/j.oceaneng.2024.117530

Zhang PY, Feng JC, Li XL, Zhang JF, Le CH, Ding HY (2023) Influence of different soil on horizontal bearing characteristics of tripod suction jacket foundations. Acta Energiae Solaris Sinica 44(4): 189-194. https://doi.org/10.19912/j.0254-0096.tynxb.2022-0270

Zhang PY, Feng JC, Shi YJ, Le CH, Ding HY (2024) Influence of length to diameter ratio of the skirt on horizontal bearing characteristics of tripod suction jacket foundation in sandy soil. Journal of Marine Science and Application 23(2): 406-416. https://doi.org/10.1007/s11804-024-00411-8

Zhang YY, Dong S, Wang QH (2011) Study on the horizontal limit bearing capacity of the deep-sea suction anchor. Journal of Ocean University of China (Natural Science Edition) 41(5): 114-119. https://doi.org/10.16441/j.cnki.hdxb.2011.05.018

Zhao L, Bransby MF, Gaudin C (2020) Centrifuge observations on multidirectional loading of a suction caisson in dense sand. Acta Geotechnica 15(1): 1439-1451. https://doi.org/10.1007/s11440-020-00970-4